Numerical methods for accurate and efficient ductile fracture predictions

Contents

5.1 Introduction 88
5.2 An uncoupled fracture model for Advanced High Strength Steel sheets 89
5.2.1 Plasticity model 89
5.2.2 Fracture model 90
5.3 Influence of Finite Element modeling on ductile fracture predictions 91
5.3.1 Methodology 93
5.3.2 Results for shell elements 94
5.3.3 Results for solid elements 97
5.3.4 Comparison shell-solid 100
5.3.5 Mixed shell-solid model 102
5.4 Dynamic shell-to-solid re-meshing 105
5.4.1 Principle 105
5.4.2 Simple example 107
5.4.3 Application to basic fracture experiments 110
5.5 Conclusion 118

Abstract

The influence of spacial discretization in FE simulations on predictions of mechanical response and ductile fracture in AHSS structures is analysed. The inability of shell elements to accurately predict the post-necking behavior of sheet materials is highligted. On the contrary predictions independent from the mesh characteristics are obtained with solid elements if sufficiently fine meshes are used. However, intensive computation efforts associated with the use of fine meshes of solid elements to model sheet structures such as automootive parts make it unsuitable to an industrial

[7] The work described in this chapter has been carried out at E.S.I. group in Rungis, France, as part of a six month part-time collaboration.

environment. A dynamic shell-to-solid re-meshing technique is considered to benefit from both the numerical efficiency of shells and the accuracy of fine solid meshes. Comparisons of numercial predictions using re-meshing to experimental results show a significant increase of the accuracy of fracture predictions compared to shell simulations, and substantial time savings compared to solid simulations.

5.1 Introduction

With the generalization of virtual engineering practices in the development and design of new vehicles, an accurate and predictive modeling of ductile fracture in sheet materials has become a significant issue. However, in an industrial context, an appropriate balance must be found between numerical efficiency and accuracy. Finite element simulations of the mechanical response of sheet structures are therefore commonly performed with shell elements, which allow for faster computations. However, fracture predictions using shell elements are often compromised by the dependence of shell models submitted to large deformation to the mesh size.

This chapter focuses on the influence of the finite element modeling on ductile fracture predictions in Advanced High Strength Steel sheets. For that purpose the influence of the type of elements used and their characteristic size is investigated. Finite element simulations of a flat notched specimen submitted to tension (which is typically used to characterize experimentally the onset of ductile fracture in sheet materials) are carried out with both shell and solid elements, with five different mesh densities. Simulation results are compared in terms of the predicted force displacement curves and the predicted displacement at which the onset of ductile failure occurs, and the local stress, strain and damage evolutions are also analyzed. Results show that in the early stages of the simulation, both shell and solid elements give comparable results, regardless of the mesh size. However fracture predictions are significantly different, depending on the mesh size and type. The critical instant after which shell elements give inaccurate results is the onset of through-the-thickness localization. After the onset of localized necking, shells are not able to predict the local stress state correctly, resulting in a spurious localization of the deformation and inaccurate and mesh-size-dependent fracture predictions. Solid elements, however, are able to predict the material evolution after the onset of necking, and give results independent from the mesh size if it is small enough. This increased accuracy is obtained at the expense of computational efficiency.

Consequently, a shell-to-solid re-meshing technique permitting to refine locally the shell mesh into solid elements during the simulations, in areas where the sheet material experiences localized necking, is presented. Improved shell simulations using re-meshing are carried out and evaluated. The accuracy of the re-meshing technique is evaluated based on numerical simulations of tensile fracture experiments and on a comparison between numerical predictions and experimental results. It is shown that the accuracy of shell simulations is increased when using re-meshing. In particular, the post-necking behavior of the sheet material can be captured correctly. In addition, using shell-to-solid re-meshing offers about 75% savings on the computational cost compared to simulations with solid elements.

In this chapter we limit our attention to low strain rate experiments and rate-independent plasticity and fracture models.

5.2 An uncoupled fracture model for Advanced High Strength Steel sheets

We make use of a rate-independent simplification of the plasticity model proposed in Chapter 4. The onset of ductile farcture will be modeled independently using the so-called Modified Mohr-Coulomb (MMC) model (Bai and Wierzbicki, 2010, [7]). The predictive capabilities of the constitutive and fracture models described thereafter are not investigated here. The reader is referred to Mohr et al. (2010, [122]) and Dunand and Mohr (2011, [49]) for a critical evaluation.

5.2.1 Plasticity model

For the present sheet material, nearly the same stress-strain curve is measured for different specimen orientations even though the r-values are direction dependent. As detailed in Mohr et al. (2010, [122]), we make use of a planar isotropic quadratic yield function,

$$f(\boldsymbol{\sigma}, k) = \bar{\sigma} - k = 0 \quad , \quad \bar{\sigma} = \sqrt{(\boldsymbol{P\sigma}) \cdot \boldsymbol{\sigma}} \tag{5-1}$$

in conjunction with a non-associated flow rule

$$\boldsymbol{\varepsilon_p} = d\lambda \frac{\partial g}{\partial \boldsymbol{\sigma}} \tag{5-2}$$

$d\lambda \geq 0$ denotes the plastic multiplier. The anisotropic quadratic flow potential reads

$$g = \sqrt{(\boldsymbol{G\sigma}) \cdot \boldsymbol{\sigma}} \tag{5-3}$$

P and **G** are symmetric positive-semidefinite matrices, with $\bar{\sigma} = 0$ and $g = 0$ if and only if $\boldsymbol{\sigma}$ is a hydrostatic stress state. The values for the non-zero components of **P** and **G** are given in Table 5-1. $\boldsymbol{\sigma}$ denotes the Cauchy stress vector in material coordinates,

$$\boldsymbol{\sigma} = [\sigma_0 \quad \sigma_{90} \quad \sigma_n \quad \tau \quad \tau_{0n} \quad \tau_{90n}]^T \tag{5-4}$$

The components σ_0, σ_{90} and σ_n represent the true normal stress in the rolling, transverse and out-of-plane directions; τ denotes the corresponding in-plane shear stress, while τ_{0n} and τ_{90n} represent the corresponding out-of-plane shear stresses. Isotropic strain hardening is described as

$$dk = h(\bar{\varepsilon}^p) d\bar{\varepsilon}^p \tag{5-5}$$

where $h = h(\bar{\varepsilon}^p)$ defines the strain hardening modulus. The strain hardening response of the material is modeled by a saturation law

$$h(\bar{\varepsilon}^p) = H_0 \left(1 - \frac{k(\bar{\varepsilon}^p)}{k_\infty}\right)^r \tag{5-6}$$

5.2.2 Fracture model

The original Mohr-Coulomb failure criterion (Mohr, 1900, [127]) is formulated in the stress space and assumes that failure occurs when the shear and normal stresses on any plane of normal vector $\boldsymbol{n}$ verify the condition

$$\max_{\mathbf{n}}(\tau + c_1\sigma_n) = c_\alpha \tag{5-7}$$

with the friction coefficient c_1 and the cohesion c_α. Bai and Wierzbicki (2010, [7]) transformed Eq. (5-7) into the space of stress triaxiality, Lode angle and equivalent plastic strain to fracture assuming proportional monotonic loading, a pressure and Lode angle dependent isotropic plasticity model, and isotropic strain hardening according to the power law. The resulting explicit expression for the fracture strain reads

$$\hat{\varepsilon}(\eta,\bar{\theta}) = \left\{c_2\left[c_3 + \frac{\sqrt{3}}{2-\sqrt{3}}\left(c^{ax}(\bar{\theta}) - c_3\right)\left(\sec\left(\frac{\bar{\theta}\pi}{6}\right) - 1\right)\right] \cdot \right.$$
$$\left.\left[\sqrt{\frac{1+c_1^2}{3}}\cos\left(\frac{\bar{\theta}\pi}{6}\right) + c_1\left(\eta + \frac{1}{3}\sin\left(\frac{\bar{\theta}\pi}{6}\right)\right)\right]\right\}^{-\frac{1}{n}} \tag{5-8}$$

with

$$c^{ax}(\bar{\theta}) = \begin{cases} 1 & \text{for } \bar{\theta} \geq 0 \\ c_{ax} & \text{for } \bar{\theta} < 0 \end{cases} \tag{5-9}$$

The exponent n describes the strain hardening of the material. The coefficient c_2 is related to c_α in Eq. (5-7), while c_3 and c_{ax} characterize the dependence of the underlying plasticity model on the third stress invariant. c_3 controls the amount of Lode angle dependence of the fracture locus and $c^{ax}(\bar{\theta})$ controls the asymmetry of the fracture locus with respect to the plane $\bar{\theta} = 0$. Despite the discontinuity of $c^{ax}(\bar{\theta})$, the fracture strain $\hat{\varepsilon}(\eta,\bar{\theta})$ is a continuous function of the stress invariants η and $\bar{\theta}$. To apply the MMC fracture model for non-proportional loadings, Bai and Wierzbicki (2010, [7]) make use of Eq. (5-8) as reference strain in Eq. (2-19).

5.3 Influence of Finite Element modeling on ductile fracture predictions

The influence of the type of elements (brick vs shell) and their characteristic dimensions are investigated on numerical simulations of a tensile experiment on a flat specimen with circular notches of radius 6.67mm, as sketched in Fig. 4-1c. Parameters for the constitutive model described in Section 5.2 have been calibrated on an extensive

Table 5-1: Material parameters for the TRIP780 steel

Yield function	F_{11} [-]	F_{22} [-]	F_{33} [-]	F_{44} [-]	F_{12} [-]	F_{13} [-]	F_{23} [-]
	1.00	1.00	1.06	2.94	-0.47	-0.53	-0.53
Flow potential	G_{11} [-]	G_{22} [-]	G_{33} [-]	G_{44} [-]	G_{12}[-]	G_{13} [-]	G_{23} [-]
	1.00	0.94	1.00	2.64	-0.47	-0.53	-0.47
Hardening	k_0 [MPa]	k_∞ [MPa]	H_0 [MPa]	r [-]			
	459	1173	20425	1.867			
MMC	c_1 [-]	c_2 [-]	c_3 [-]	c_{ax} [-]	n [-]		
	0.3472	0.9098	1.7003	1.546	0.204		

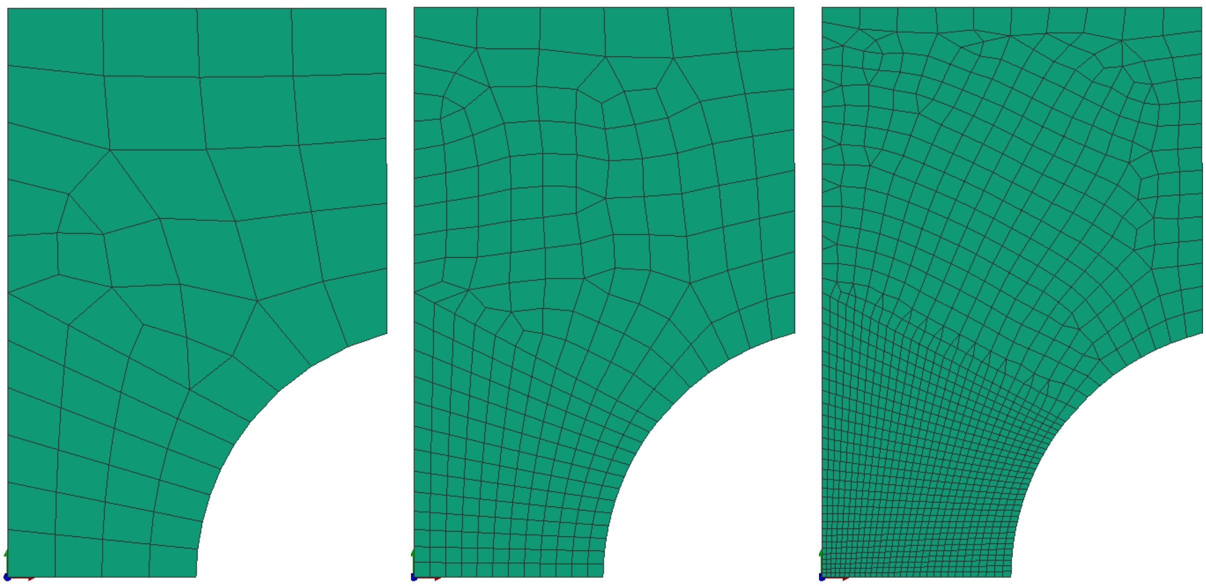

(a) (b) (c)

Figure 5-1: Meshes of the notched tensile specimen. (a) very coarse mesh; (b) medium mesh and (c) very fine mesh.

set of multi-axial fracture experiments carried out on TRIP780 steel (Mohr et al., 2010, [122]; Dunand and Mohr, 2011, [49]). Note that this material comes from a different production batch than the one used in Chapters 3, 4 and 6. Materials parameters are thus slightly different.

5.3.1 Methodology

Finite element simulations are run with five different mesh densities, shown in Fig. 5-1:

(i) very coarse mesh with an element edge length of $l_e = 1250\mu m$ at the specimen center and $n_t = 1$ elements in thickness direction (half thickness),

(ii) coarse mesh with $l_e = 830\mu m$ and $n_t = 2$;

(iii) medium mesh with $l_e = 415\mu m$ and $n_t = 4$;

(iv) fine mesh with $l_e = 200\mu m$ and $n_t = 8$;

(v) very fine mesh with $l_e = 100\mu m$ and $n_t = 12$.

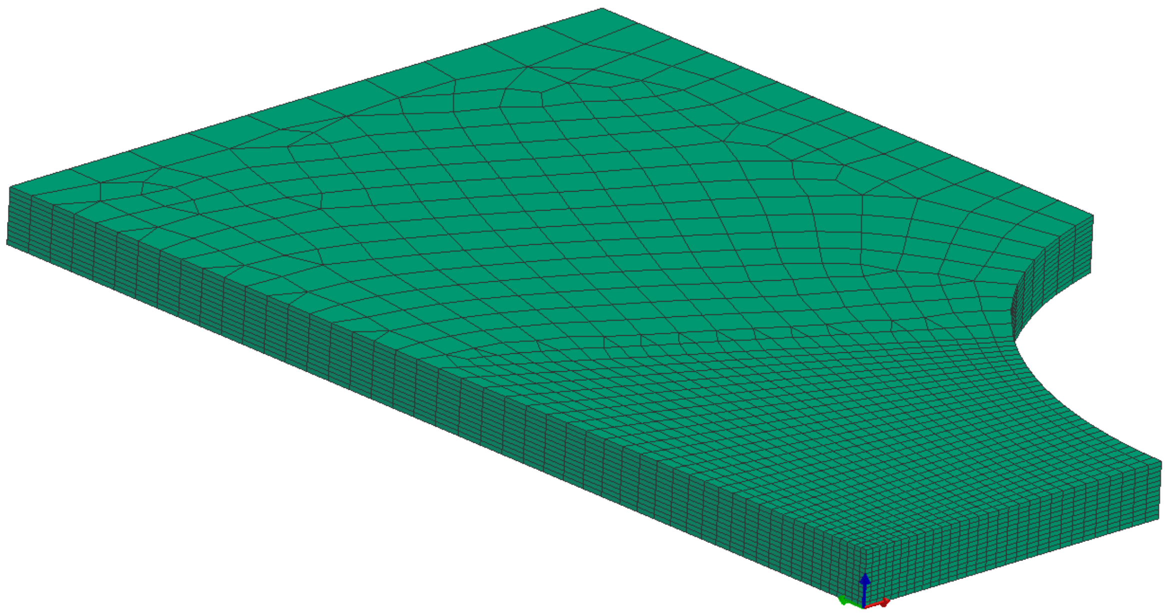

Figure 5-2: View of the very fine mesh with 12 solid elements through the half-thickness

Note that the medium shell mesh corresponds to current standard practices in industrial simulations of car crash tests. Meshes with both only shell and only solid elements are considered. For a given density, shell and solid meshes are identical in the sheet plane. Only the number of elements through the thickness varies (1 for shell, $2n_t$ for solids). Because of the symmetries of the notched specimen, only $1/4$ of the specimen is meshed, and half the thickness for solid meshes. A displacement boundary condition is imposed to the upper boundary of the specimen (constant velocity). All simulations are run up to an imposed displacement of 1.5mm. Fracture is assumed to occur when the critical damage $D = 1$ is reached at any integration point in the model. Note that element deletion is not used in the present simulations.

5.3.2 Results for shell elements

Force displacement curves predicted with the five meshes are depicted in Fig. 5-3. The instant at which fracture occurs is highlighted by a solid square on each curve. After the maximum of force is reached (which corresponds to the onset of localization of the plastic flow through the thickness of the specimen (localized necking)), simulation results show a very strong dependence to mesh size. More specifically, the finer the mesh, the more abrupt the force decreases after necking and the smaller the fracture displacement. It must be noted that simulation results do not converge as the mesh is refined. For most of the mesh densities, fracture occurs earlier than in the experiment. With the very fine mesh, fracture occurs in the simulation just after the maximum of force is reached.

Figure 5-4 compares the evolution of damage (solid line) and equivalent plastic strain (dashed line) at the center of the specimen for the very fine (in red) and very coarse mesh (in black). Both simulations give the same results before the maximum of force (displacement smaller than 0.8mm). But after the maximum of force, the evolution of damage and plastic strain strongly depends on the mesh size. For the very fine mesh, damage exhibits a sharp increase after necking, leading to an almost instantaneous fracture after the maximum of force.

Regardless of the element dimensions, all the deformation localizes in a band of 1 element width at the center of the gage section after the maximum of force is reached,

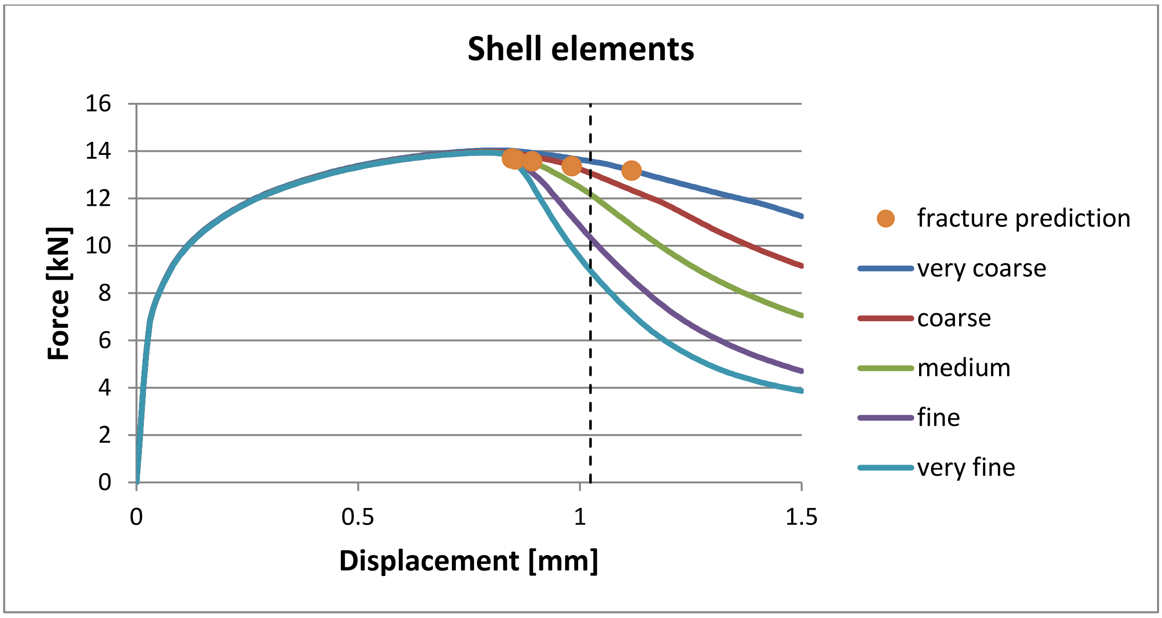

Figure 5-3: Predicted force displacement curves with shell elements. The predicted instant of fracture is shown by a solid circle for each simulation. The experimental instant of fracture is depicted by a dashed black line.

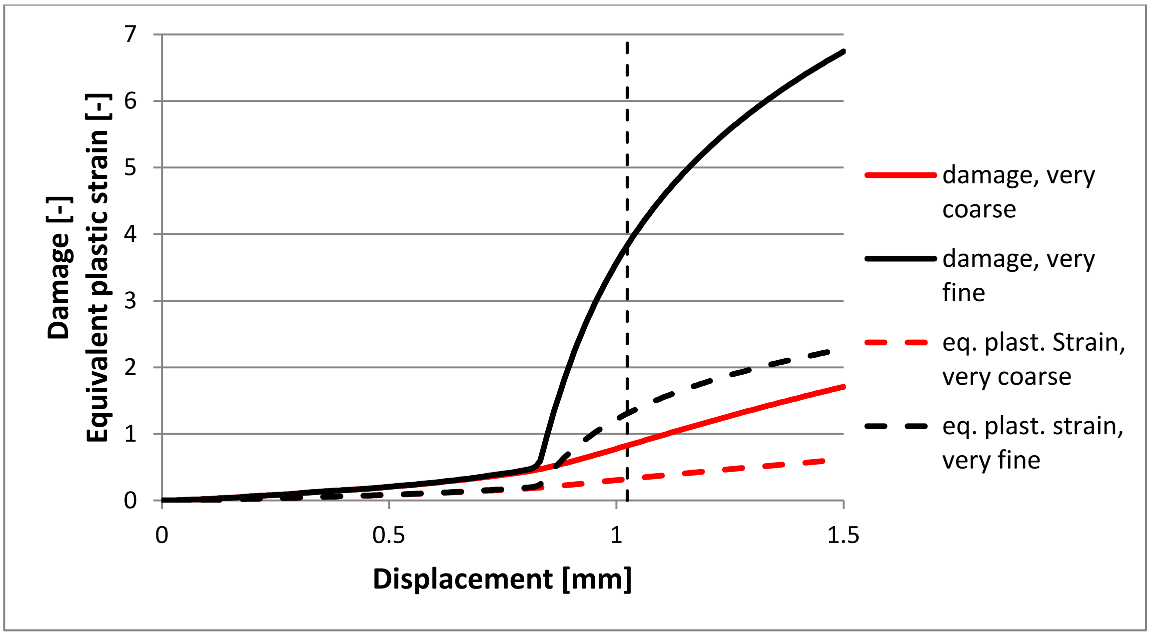

Figure 5-4: Evolution of damage and equivalent plastic strain at the center of the notched specimen, for the very fine (red) and very coarse (black) meshes with shell elements. The experimental instant of fracture is depicted by a dashed black line.

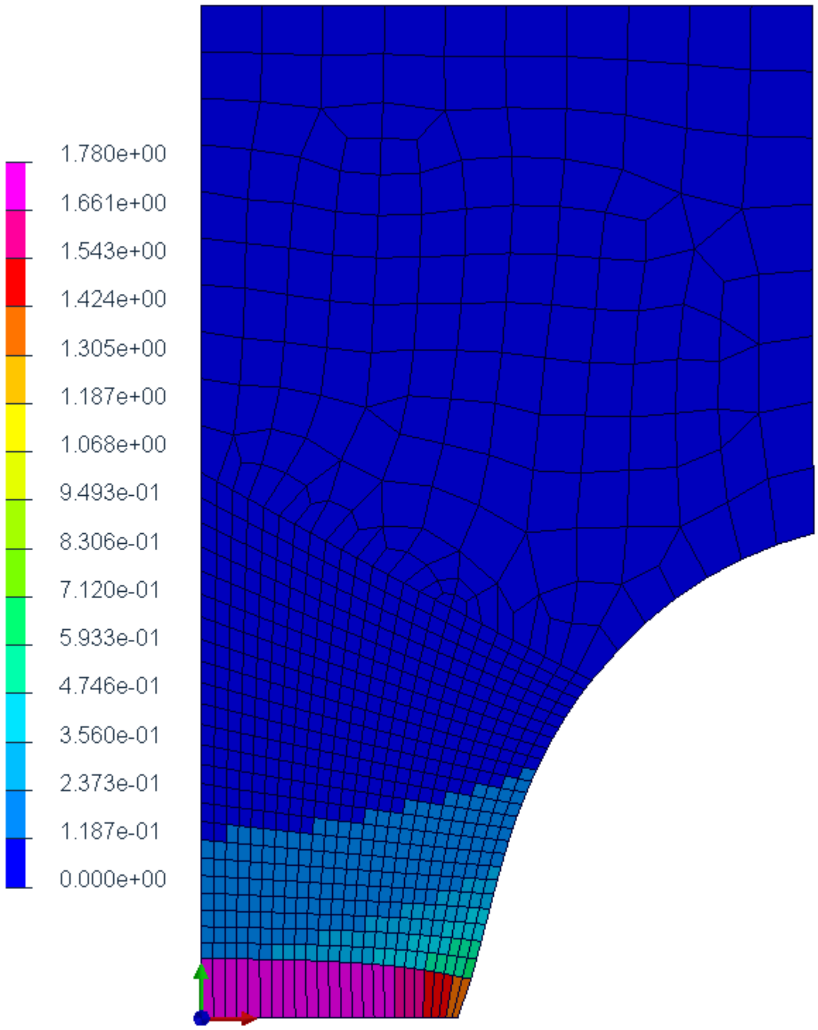

Figure 5-5: Contour plot of equivalent plastic strain after the maximum of force , using a fine mesh of shell elements

as illustrated in Fig. 5-5. This spurious localization leads to very high values of strain and damage inside that band, so that fracture occurs right after the maximum force when using fine meshes.

After necking, a three dimensional stress state develops in the material. In particular, through-the-thickness stresses appear and permit to bring additional strain hardening capabilities that is needed to compensate sheet thinning. However those mechanisms cannot be captured by shell elements, in which the state of stress is necessarily plane stress. As a result, shells cannot predict correctly the material evolution (stress and strain state) after necking, regardless of the element size. To illustrate this point, Fig. 5-6 depicts the evolution of the stress triaxiality and equivalent plastic strain at the center of the specimen, when a medium mesh is used. After necking (at an equivalent plastic strain of about 0.2), the stress triaxiality increases but rapidly saturates at a value of $\eta = 0.57$, which corresponds to transverse plane strain tension: it is the maximum of triaxiality achievable under plane stress with traction applied in only one direction. However, in the actual specimen, higher triaxialities are reached, because of the three dimensional stress state that develops.

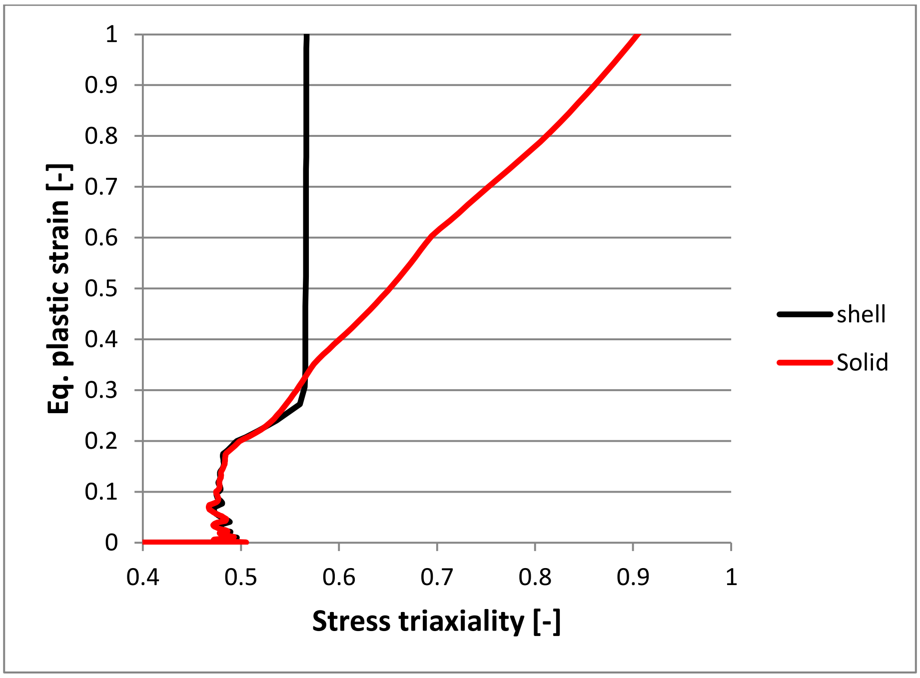

Figure 5-6: Evolution of the stress triaxiality and the equivalent plastic strain at the center of the specimen, as predicted by a fine mesh of shell elements (black line) and solid elements (red line).

5.3.3 Results for solid elements

Force displacement curves predicted with the five different solid meshes are depicted in Fig. 5-7. The instant at with fracture occurs is highlighted by a solid square on each curve. All simulations predict the same force displacement curve before the maximum of force, but some differences become noticeable thereafter. However, it should be noted that the medium, fine and very fine mesh predict the same force res-

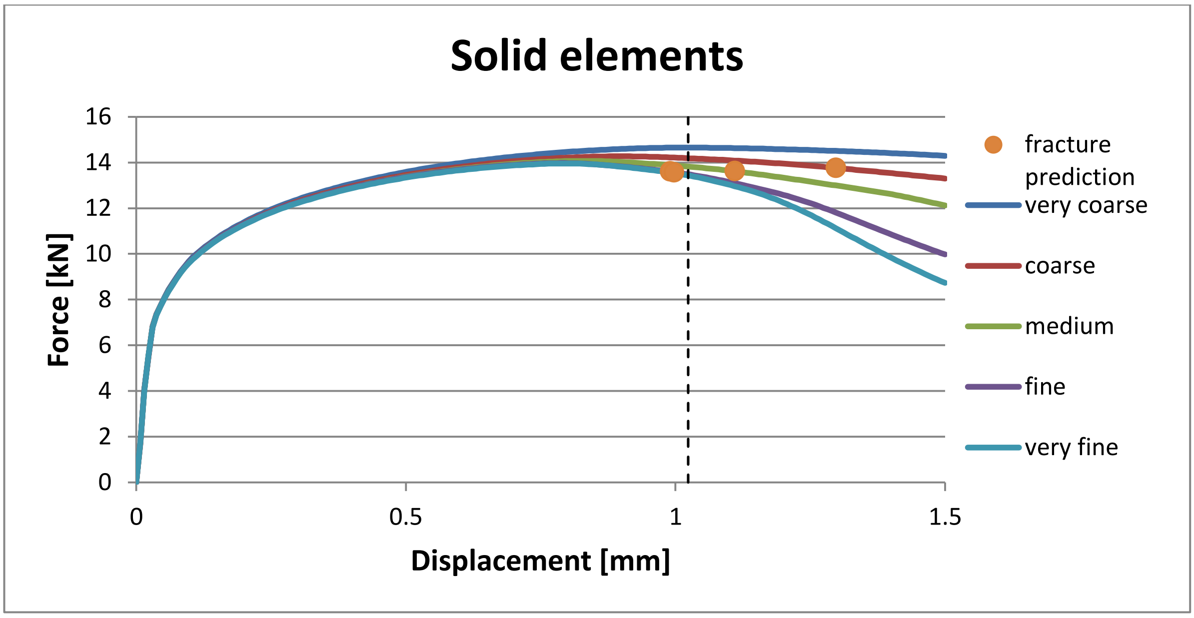

Figure 5-7: Predicted force displacement curves with solid elements. The predicted instant of fracture is shown by a solid circle for each simulation. The experimental instant of fracture is depicted by a dashed black line.

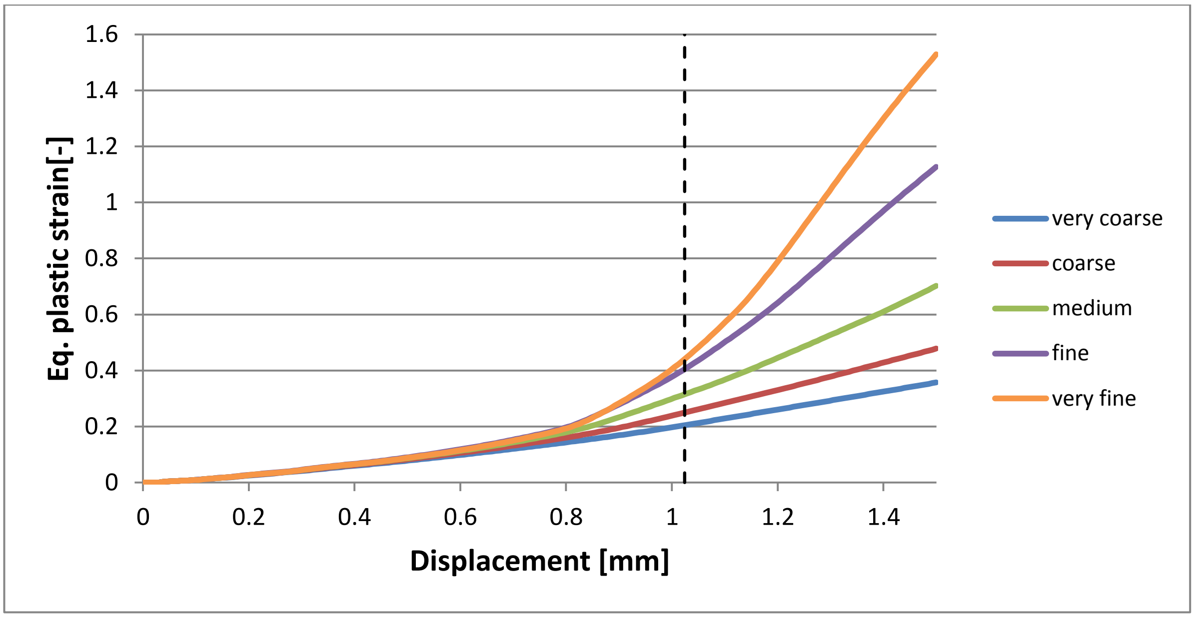

Figure 5-8: Evolution of the equivalent plastic strain at the center of the gage section for different mesh densities. The experimental instant of fracture is depicted by a dashed black line.

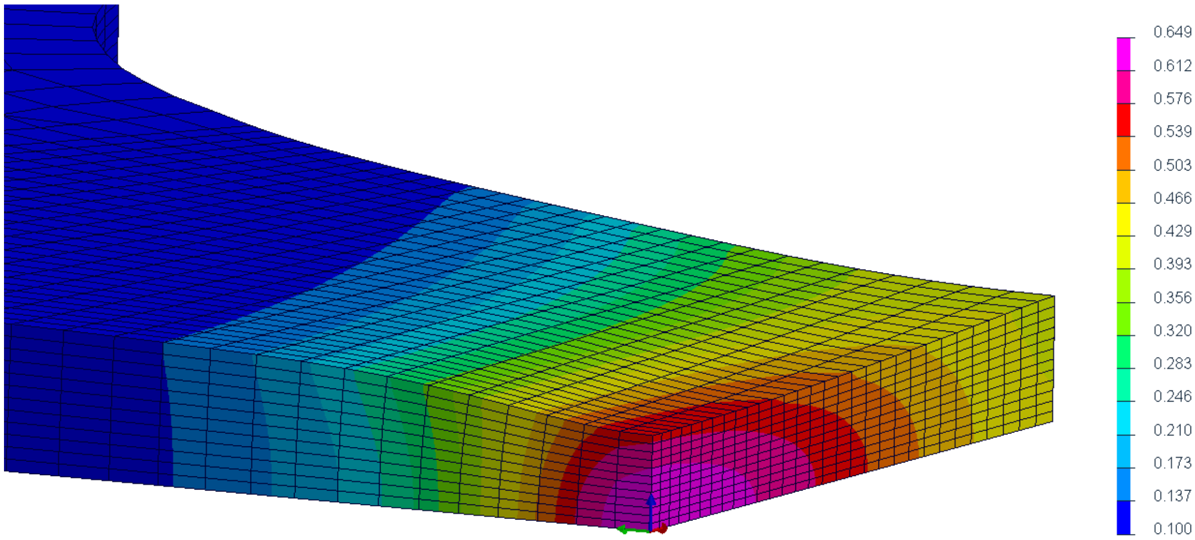

Figure 5-9: Contour plot of equivalent plastic strain after the onset of localized necking, with the very fine solid mesh.

ponse up to a displacement of 1mm, while the fracture displacement is 1.03mm: results converge as the mesh is refined. Similarly, the predicted fracture displacement decreases as the mesh is refined, but eventually converges: almost the same fracture displacement is predicted by the fine and very fine mesh.

The evolution of the equivalent plastic strain at the center of the gage section is depicted for all five mesh densities in Fig. 5-8. As for force-displacement curves, all curves are identical for displacements lower than 0.8mm, which corresponds to the maximum of force. After that instant, results become mesh size-dependent: the finer the higher, the steeper the increase of equivalent plastic strain. However, at least in the range of displacements lower than the experimental fracture displacement (black dashed line in Fig. 5-8), results converge as the mesh is refined: for displacements lower than $1mm$, the evolution of equivalent plastic strain is the same with the fine and very fine meshes.

The force displacement curves depicted in Fig. 5-7 exhibit a maximum of force (for a displacement of about 0.8mm). This maximum corresponds to the onset of localized necking at the center of the specimen gage section. As shown in Fig. 5-9, localized necking provokes a severe thickness reduction at the center of the specimen, and through-the-thickness gradients in the stress and strain fields. In addition, a three dimensional stress state develops, with significant out-of plane stresses building up.

Solid meshes with more than 1 layer of elements in the thickness direction can predict the three dimensional stress states that develops in the material after the onset of localized necking. Figure 5-6 depicts the evolution of equivalent plastic strain and stress triaxiality at the center of the specimen with a fine solid mesh (in red). The simulation is able to capture the increase of stress triaxiality after necking due to the building-up of out-of-plane stresses.

5.3.4 Comparison shell-solid

Before the onset of necking, shell and solid elements give the same results, regardless of the mesh density. Differences between mesh types and mesh densities become noticeable – and significant – only after the onset of through-the-thickness necking.

Figure 5-10 shows the predicted fracture displacement as a function of the mesh characteristic length. With both shell elements and solid elements, the prediction of fracture displacement seems to converge with respect to mesh size: the fine and very fine meshes lead to same results. In case of solid elements, the converged result is very close to the experimental displacement to fracture. However, in case of shell elements, the prediction for the fracture displacement converges towards the value of displacement at which the maximum of force occurs, which means that the accuracy of fracture predictions using shell elements cannot be increased by “tuning” the material parameters of the fracture model.

Table 5-2: CPU time (in s) for different mesh types and densities

	Very coarse	Coarse	Medium	Fine	Very fine
Shell	5.4	16	39	241	616
Solid	5.9	31	215	2913	11346

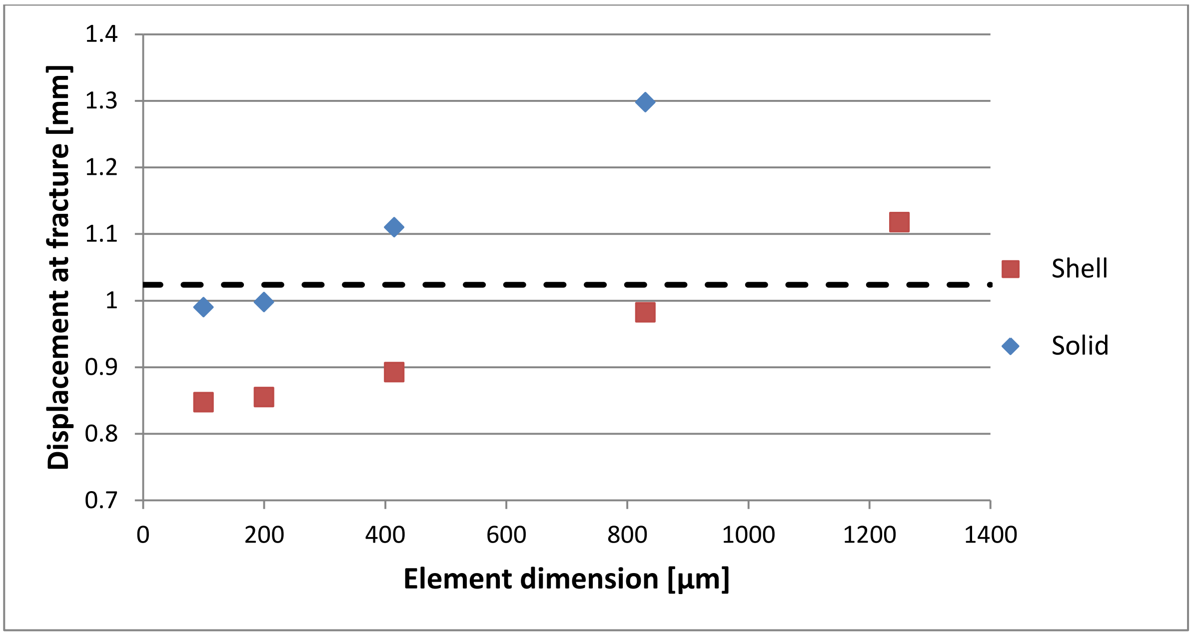

Figure 5-10: Predicted displacement at which fracture occurs with shell (red) and solid (blue) elements, for different mesh densities.

The additional accuracy of fine solid meshes comes at the expense of a prohibitive computational cost, as shown in Table 5-2. In order to get an accurate fracture prediction and converged results (fine mesh of solid elements), the computation time is 200 more important than with meshes currently used in crash simulations (medium mesh of shell elements).

To summarize:

- Shell and solid elements provide same results before through-the-thickness localization of the stress and strain fields,
- After the onset of localization,
    - Shell elements cannot predict correctly the local stress and strain state.
    - Shell elements give results (loads predictions, evolution of plastic strain and damage…) that are strongly dependent on the mesh size, and results do not converge as the mesh is refined.
    - Solid elements can predict correctly the local stress and strain state.

- Solid elements give results (fracture prediction, loads predictions…) that dependent on the mesh size if the meshes are too coarse, but results do converge when the mesh is refined.

It is clear that shell elements cannot be used to get accurate fracture predictions. In most fracture criteria, the increase of damage during straining depends on the local stress state and the evolution of plastic strain, which are not captured correctly by shells after the onset of localized necking. Moreover, it seems not possible to get predictive fracture results with shells because of the spurious localization and strong mesh density dependence of shell simulations. Results depend on mesh size, and mesh size that give most accurate results depends on the problem that is investigated: defining a "recommended shell size" could be done when investigating well known cases, but may not be applied to different geometries and/or loading conditions and/or materials.

Solid element meshes, with an element size of $200\mu m$ or less, give converged and accurate results. With such meshes, the accuracy and predictive capabilities of the simulations depend mostly on the fracture criterion itself, and no more on the finite element modeling. However such fine meshes lead to a significant increase in the computation time.

5.3.5 Mixed shell-solid model

Since the main issue with shell elements is their inability to predict the post-necking behavior of the sheet material, a possible improvement would be to use a mixed shell-solid model, where most of the specimen is meshed with shell elements (for computational efficiency) and only the area that might experience localize necking is meshed with solids. Such a mixed mesh is shown in Fig. 5-11. Here a fine mesh density, with $2n_t = 16$ elements through the total sheet thickness is used.

Special care is required to connect shell and solid elements in that model. The mesh is made such that at the interface, to all nodes from solid elements corresponds a node from a shell element. Therefore the in-plane displacements of all nodes from solids are constrained to be equal to the in-plane displacements of the corresponding node from a shell (here the specimen is not submitted to bending). No displacement constraint in the thickness direction is imposed, to allow for thickness reduction.

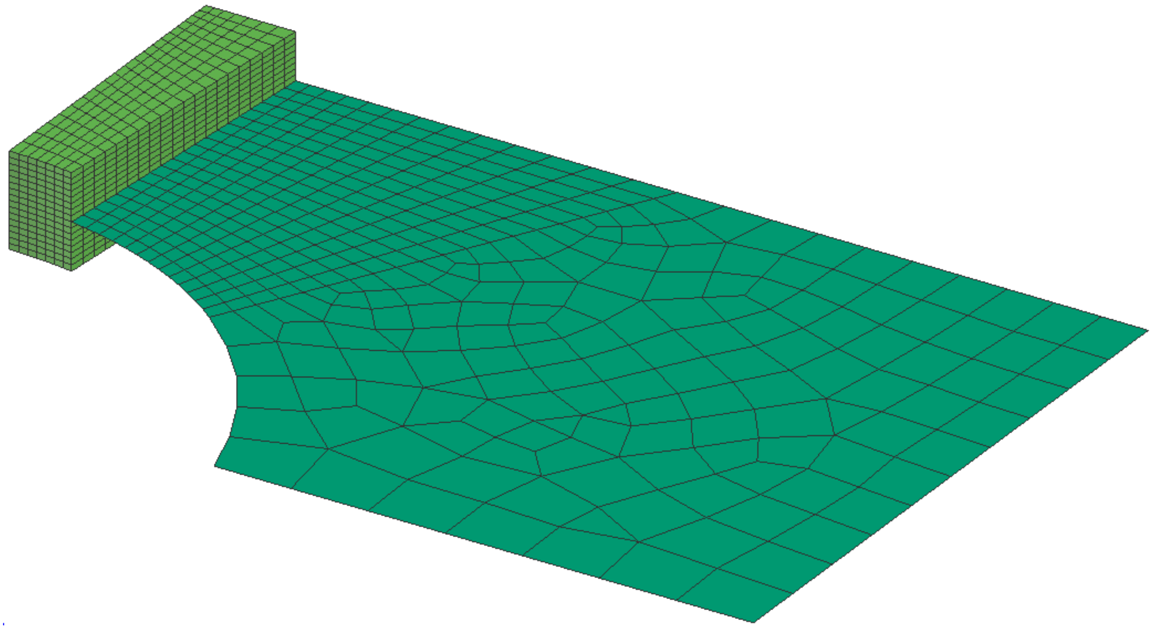

Figure 5-11: Mixed mesh with local refinement of solid elements.

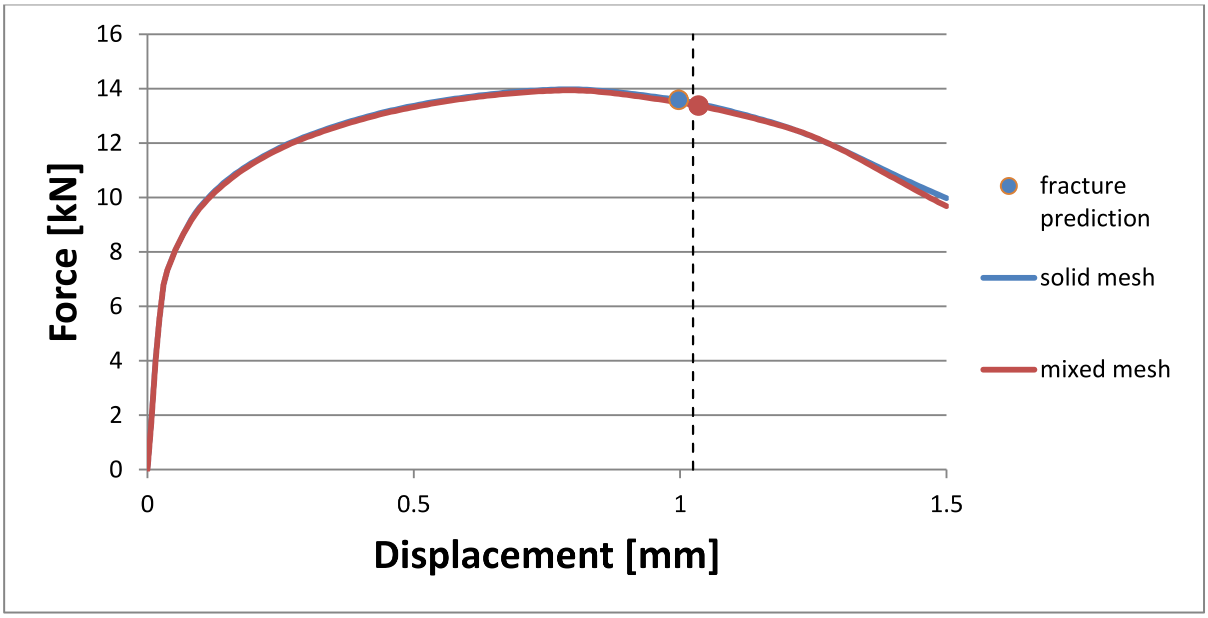

Figure 5-12: Force displacement curves and fracture predictions using a solid mesh and a mixed mesh. The experimental instant of fracture is depicted by a dashed black line.

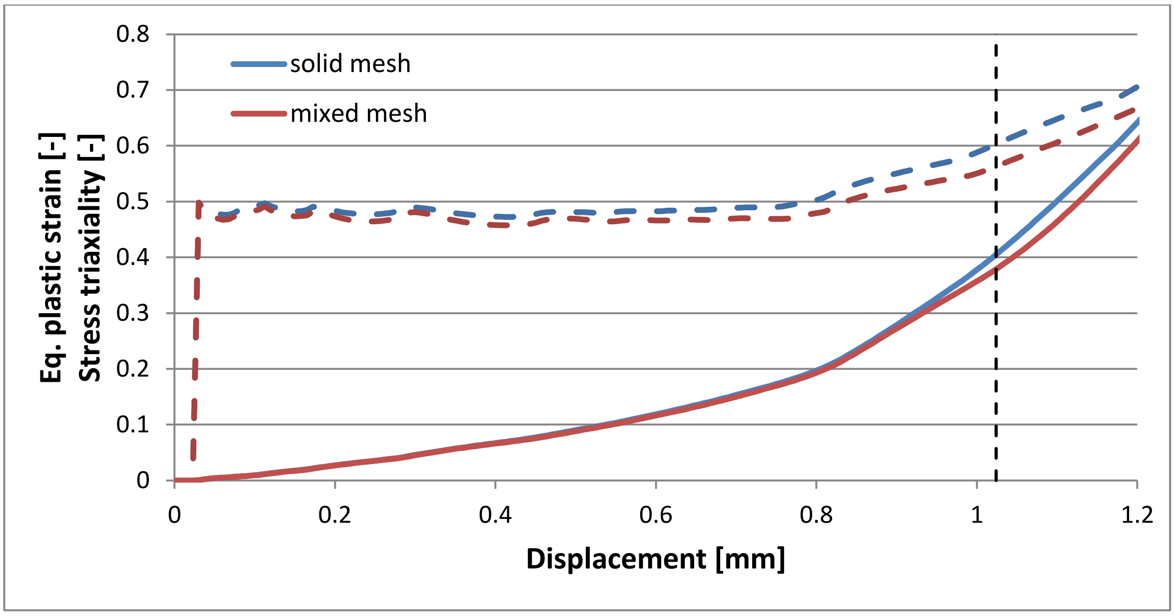

Figure 5-13: Evolution of equivalent plastic strain (solid lines) and stress triaxiality (dashed lines) at the center of the gage section, with a solid mesh (in blue) and a mixed mesh (in red). The experimental instant of fracture is depicted by a dashed black line.

Figure 5-12 depicts the force-displacement curves obtained with the fine solid mesh (in blue) and with the mixed mesh (in red). Both curves lie almost perfectly on top of each other, demonstrating that the mixed model is able to predict the load carrying capacity of the specimen, even after the onset of localized necking. Predictions of the fracture displacement are also very close in both models, only differing by about 3%. Local stress and strain states at the center of the specimen gage section are depicted in Fig. 5-13 for both models. Even though the evolution of equivalent plastic strain (solid red line in Fig. 5-13) is similar in both models up to the onset of fracture, the mixed model tends to underestimate the stress triaxiality (dashed red line in Fig. 5-13), leading to a different accumulation of damage and, *in fine*, a slightly different prediction for the fracture displacement.

The mixed model leads to results that are very close to a full solid model, at a better computational cost. The CPU time to compute the mixed model is only half that of the solid model, as shown in Table 5-3. Yet, an obvious limitation of this mixed approach is that one needs to know where localization will occur a priori, in order to mesh correctly and efficiently the model.

Table 5-3: CPU time (in s) for the solid and mixed models

Solid model	Mixed model
2913	1581

5.4 Dynamic shell-to-solid re-meshing

It has been shown that solid elements are required in the post-necking range to get accurate simulation results and fracture predictions, while shell elements give satisfactory results before the onset of necking at a much lighter cost. A solution to reduce further the computation time without compromising the accuracy of the fracture predictions would thus be to start from a mesh of only shell elements and switch locally to solid elements where localization is likely to occur. This dynamic re-meshing from shell to solid elements has been implemented in the explicit Finite Element solver PamCrash (ESI Group, [144]). The goal of the present section is to perform an assessment of this re-meshing technique in terms of result accuracy and computational efficiency.

5.4.1 Principle

The principle of the shell-to-solid re-meshing technique is described in Fig. 5-14, which corresponds to the simulation of a tension test. Starting from a very coarse shell mesh (Fig. 5-14a), the shell elements in the specimen gage section are transformed into finer solid elements when a critical equivalent plastic strain is reached (Fig. 5-14b and 5-14c). All local state variables (stresses, strains…) are automatically mapped from the integration points of the shell element to the integration points of the new solid mesh. Note that all the solid elements replacing a single shell elements and located in the same layer in the sheet plane are initialized with the same value for all state variables

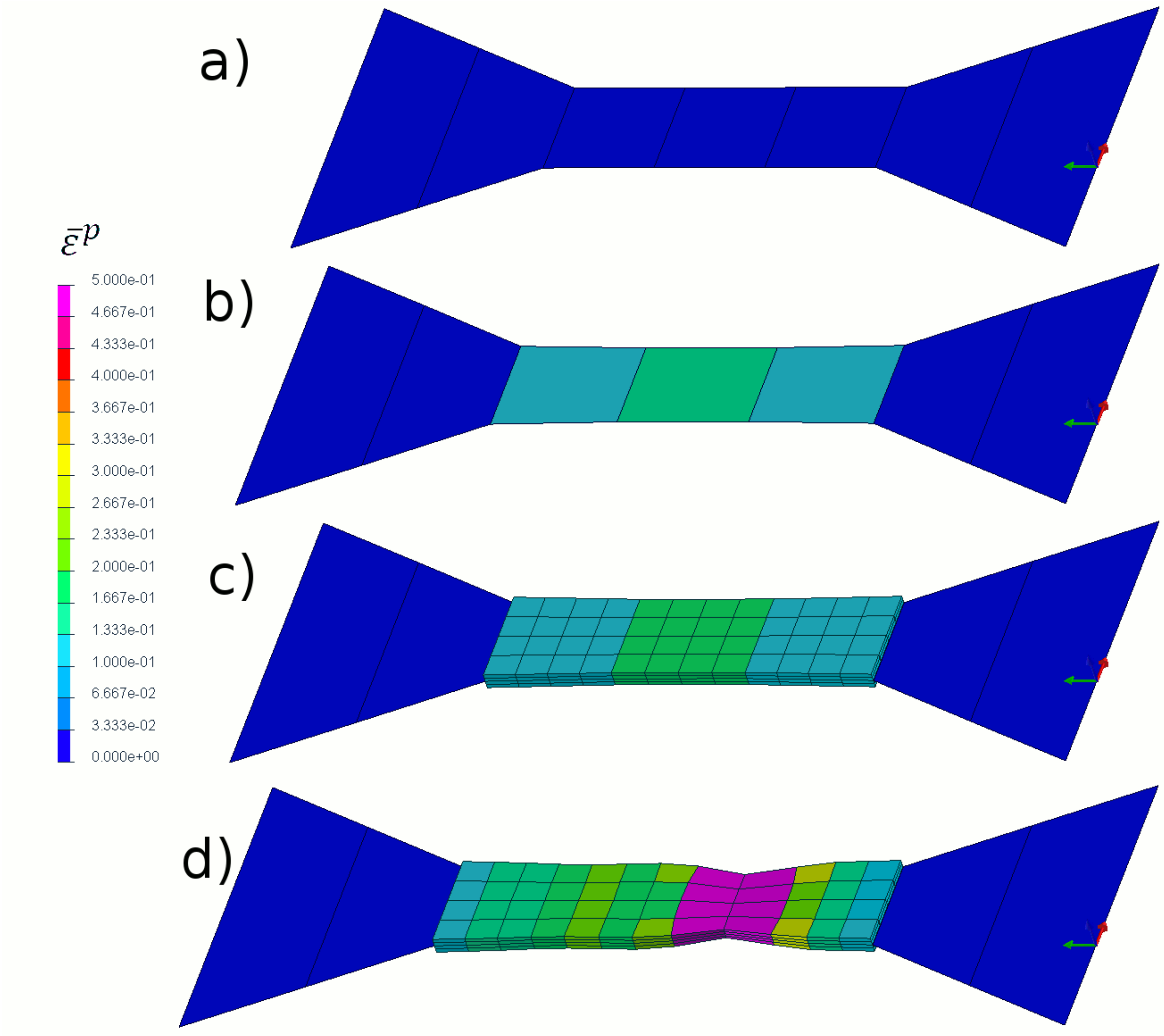

Figure 5-14: Simulation of a tension test using shell-to-solid re-meshing. (a) initial mesh; (b) Before the re-meshing step; (c) after the re-meshing step and (d) neck development.

(as can be seen in Fig. 5-14 for the equivalent plastic strain): there is no in-plane interpolation of the local fields between different integration points. However interpolation is performed in the through-the-thickness direction, as a shell typically features multiple integration points through the thickness, which do not necessarily match the number of generated solids in the thickness direction. This method permits to correctly account for bending deformations and bending moments during the re-meshing process. A localized neck is then able to develop within the solid mesh (Fig. 5-14d).

Shell-to-solid re-meshing has two major effects on computational time:

- It increases significantly the total number of degrees of freedom and element integration points of the model,
- In an explicit time integration scheme, newly generated solid elements are associated to a stable time increment much smaller than that of the shell elements they are replacing, being of smaller dimensions.

In order not to penalize the complete model with a reduced time increment, and since re-meshing often only concerns a small region of the model geometry, solid elements are isolated in a separate sub-model. A multi-model coupling technique then permits to use different time increments for the shell and solid elements [144]. In this case, nodes located at the interface of shell and solid elements are linked with non-linear springs, in order to transmit loads and velocities while running on different time increments.

Plasticity and fracture models defined in Section 5.2, and the routines needed to map relevant variables (stresses, strains, damage indicator) from shell elements to solid elements during re-meshing have been implemented into the Finite Element software PamCrash to carry out the work described thereafter.

5.4.2 Simple example

Before analyzing complex fracture problems, we start by evaluating the shell-to-solid re-meshing technique on a simulation of a simple tension test on a sheet specimen, as shown in Fig. 5-14.

5.4.2.1 Numerical model and results

The initial shell model of the tension specimen is depicted in Fig. 5-14a. The gage section is 30mm long and 10mm wide and is meshed with only three shell elements. To load the specimen, displacements are imposed to one boundary, while the other is fixed. A non-associated quadratic plasticity model, as described in section 5.2, is used along with the material parameters given in Table 5-1. No fracture criterion is used so far.

The shell-to-solid re-meshing option is activated. When an equivalent plastic strain of $\varepsilon^p = 0.18$ is reached at any integration point of a shell element, it is replaced by solids. Each re-meshed shell is decomposed into 4 solid elements in each in-plane direction, and 4 elements in the thickness direction, as shown in Fig. 5-14c.

The resulting load-displacement curve is depicted with a blue line in Fig. 5-15. The instant when re-meshing occurs is characterized by a significant spike in the applied load, followed by an almost complete drop of the load. The applied load comes back to the level before re-meshing only after an additional imposed displacement of about 0.2mm. In between, the model deforms purely elastically. After some plastic deformation of the generated solid elements, a diffuse and then localized neck forms in the solid mesh, as visible in Fig. 5-14d. This neck leads to a smooth decrease of the applied load, as described in the previous section.

During the re-meshing step, springs that link shell and solid models are created with zero internal load, while they replace material that was loaded up to its yielding point. Therefore this transient behavior corresponds to a transfer of load between the initially unloaded springs and the elastically loaded shell and solid elements. It ends when the model reaches equilibrium, i.e. when the level of load applied before re-meshing is attained.

The evolution of the kinetic energy in the model in shown in Fig. 5-16. Clearly, the total kinetic energy is higher after re-meshing. This additional energy comes from the additional mass introduced by the springs created to link the shell and solid elements models. In this specific simulation, the mass of the springs (which is chosen automatically by the solver based on stability criteria) is twice the mass of the generated solid elements. In addition a transient period exists right after re-meshing, where the kinetic energy in the solid model exhibits very large oscillations. This transient corresponds to the time the springs initialized with a zero velocity need to reach equilibrium (constant non-zero velocity). Note that a constant velocity is imposed to the boundaries of the model.

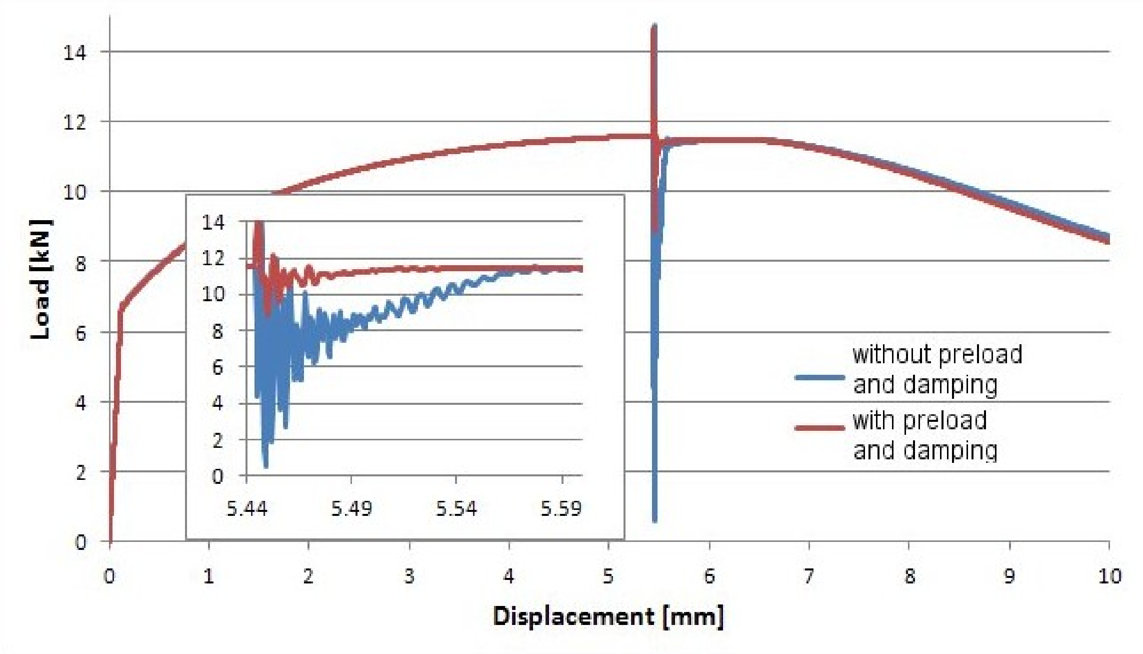

Figure 5-15: Force displacement curve of a tensile test with re-meshing, with (red) or without (blue) pre-load and damping.

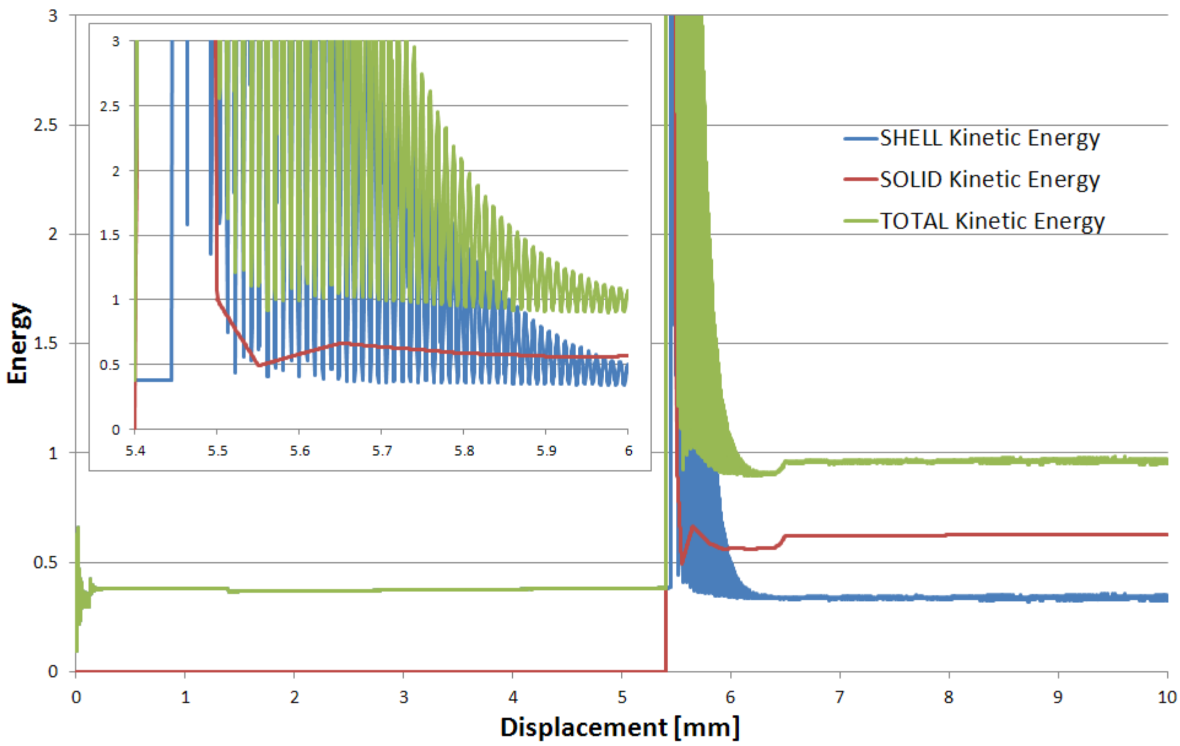

Figure 5-16: Evolution of the model kinetic energy.

5.4.2.2 Influence of modeling parameters

Different parameters are implemented to reduce the transient following the re-meshing step:

- Pre-load can be introduced in the springs,
- Proportional damping and non-linearity can also be introduced in the spring behavior.

An initial load is introduced in the springs linking nodes from the shell model and nodes from the solid model. The pre-load is chosen equal to the contribution to the nodal force coming from elements that are being re-meshed at the instant of re-meshing. In addition, proportional damping in the spring permits to reduce the oscillations of kinetic energy visible in Fig. 5-15. The force-displacement curve obtained using both pre-load and damping is shown in red in Fig. 5-15. The drop of force at the instant of re-meshing, as well as resulting oscillations, are significantly reduced.

Similarly, defining a non-linear behavior for the spring (so that the spring load is no more proportional to its elongation) can help reduce the transient to a small extent. This type of behavior penalizes an excessive extension or compression of the spring. However it has been found that using a non-linear behavior has much less influence on the transient than pre-loading the spring or using damping.

5.4.3 Application to basic fracture experiments

The next step in assessing the performances of the re-meshing technique consists of comparing its predictions against real fracture experiments.

5.4.3.1 Experiments

We use experimental results described in [48]. In this work, tensile experiments have been performed on three different specimen geometries sketched in Fig. 5-17: notched tensile specimens with a notch radius of $R = 6.65mm$ and $R = 20mm$, respectively, and a tensile specimen with a $8mm$ diameter central hole. The central

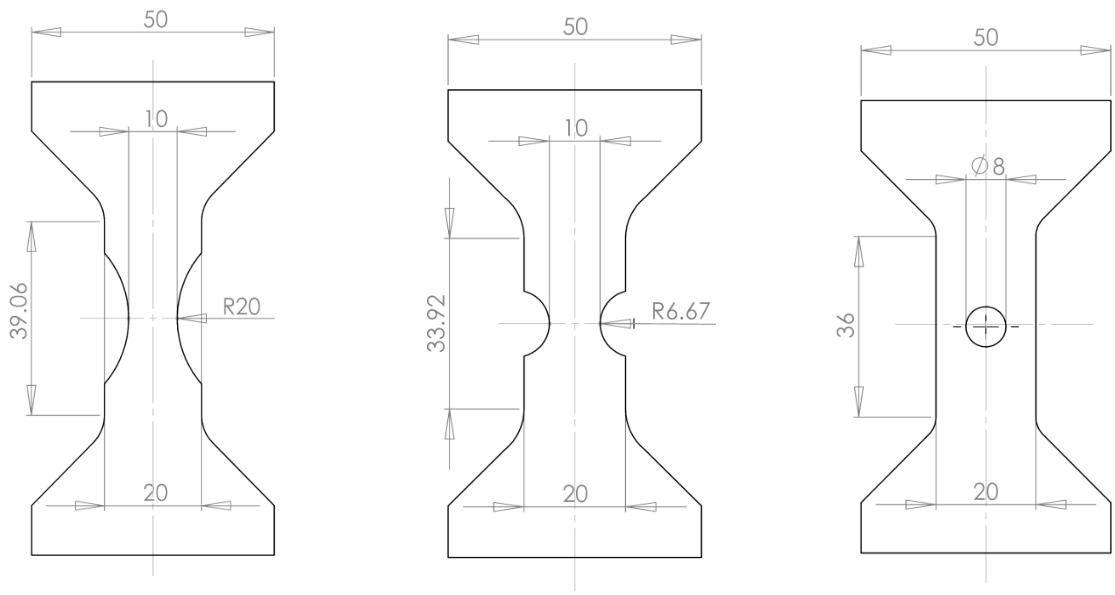

Figure 5-17: Flat tensile specimens with different notched radii and with a central hole.

hole specimen permits to characterize the onset of ductile fracture under a state of uniaxial tension, while notched tensile specimens allow for fracture characterization under higher triaxialities. All experiments are performed on a TRIP780 Advanced High Strength steel sheet, whose material characterization is given in Table 5-1.

5.4.3.2 Numerical models

For each specimen, we consider three different numerical simulations:

1. The geometry is meshed with a coarse mesh of shell elements (as described in Section 5.3: shells are $0.8mm$ long in each direction). The re-meshing capability is switched off.
2. The geometry is initially meshed the shell elements, with the same density as in case 1. The re-meshing capability is switched on: when an equivalent plastic strain of 0.18 is reached at any integration point of a shell, this element and its neighbors (in a region of 5mm radius) are replaced by solid elements. Each shell is replaced by 4x4 solid elements in both in-plane directions, and 16 elements in the thickness direction. The density of solid elements corresponds

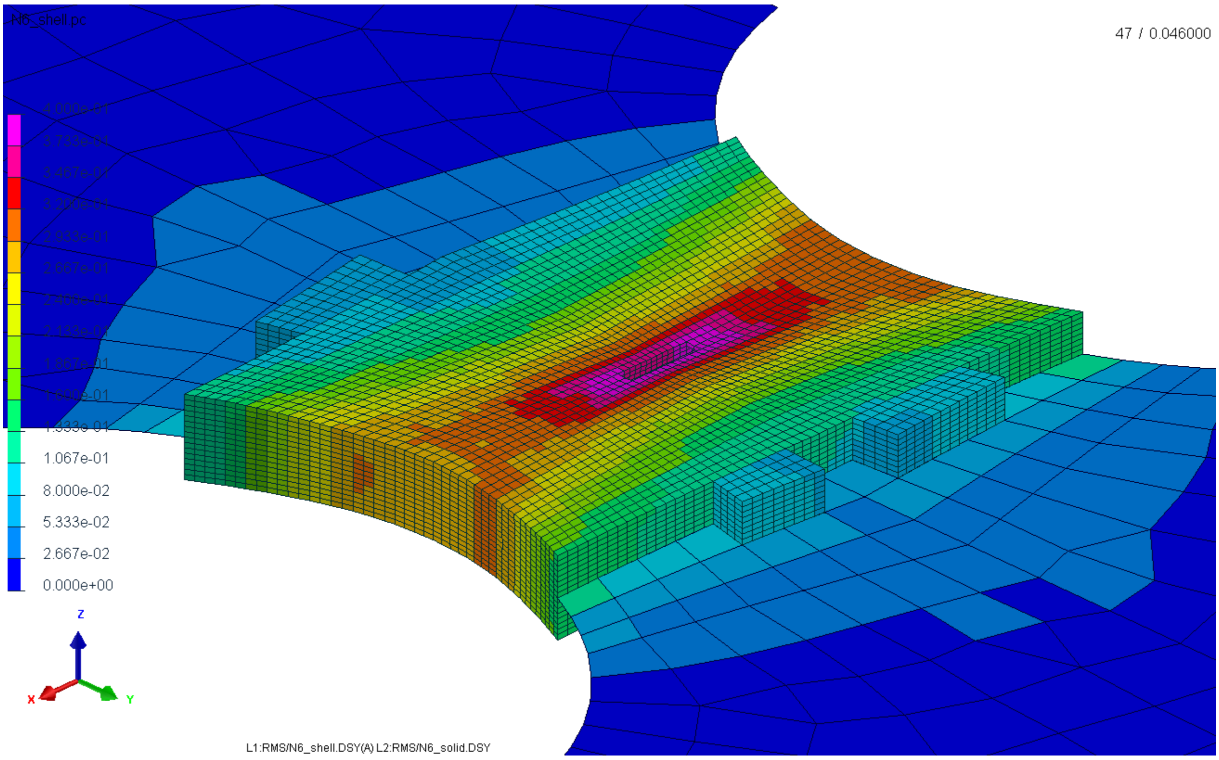

Figure 5-18: Contour plot of equivalent plastic strain in a $6.65mm$ notched tensile specimen after re-meshing of the gage section center. Central elements have already failed.

to that of the fine mesh described in Section 5.3, with an in-plane length of $200\mu m$ and thickness of $100\mu m$.

3. The geometry is meshed with solid elements only. The density corresponds to the one obtained after re-meshing in case 2.

We make use of the modeling parameters that have been recommended previously for the re-meshing operation. In all simulations, element deletion is performed when a damage value of 1.0 is reached at any integration point of an element.

5.4.3.3 Results and discussion

Figure 5-18 shows the result of the re-meshing procedure for the $6.65mm$ notched tensile specimen. All the shell elements located at the center of the gage

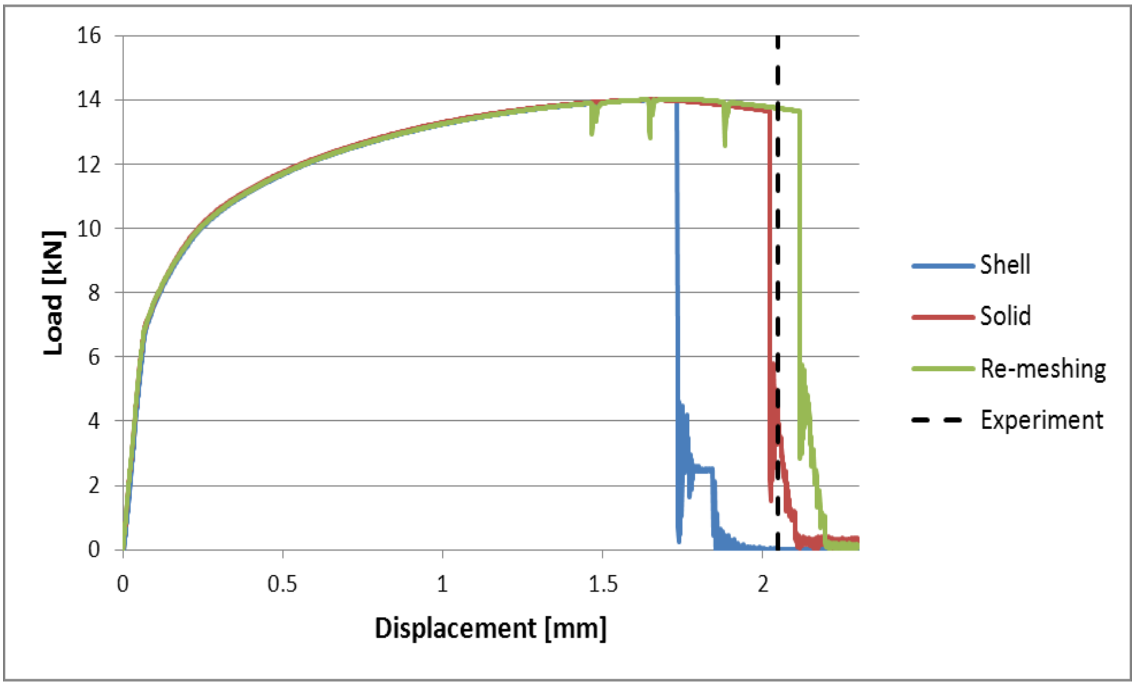

Figure 5-19: Predicted force displacement curve of the $6.5mm$ notched tensile test with re-meshing. The experimental instant of fracture is depicted by a dashed black line.

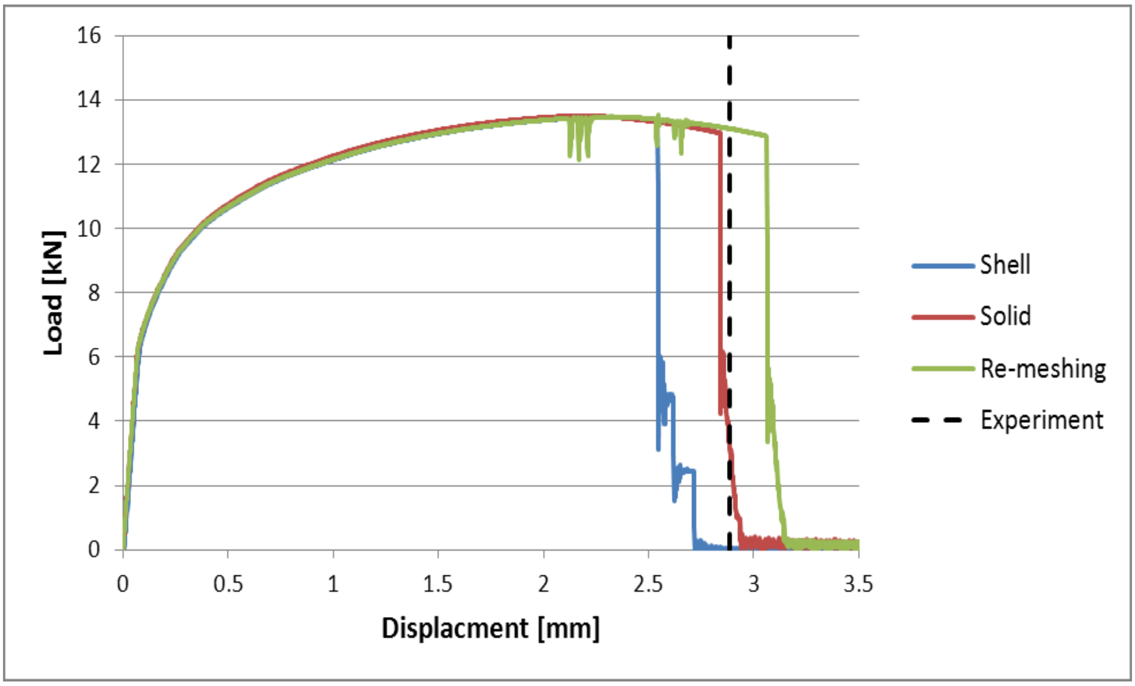

Figure 5-20: Predicted force displacement curve of the $20mm$ notched tensile test with re-meshing. The experimental instant of fracture is depicted by a dashed black line.

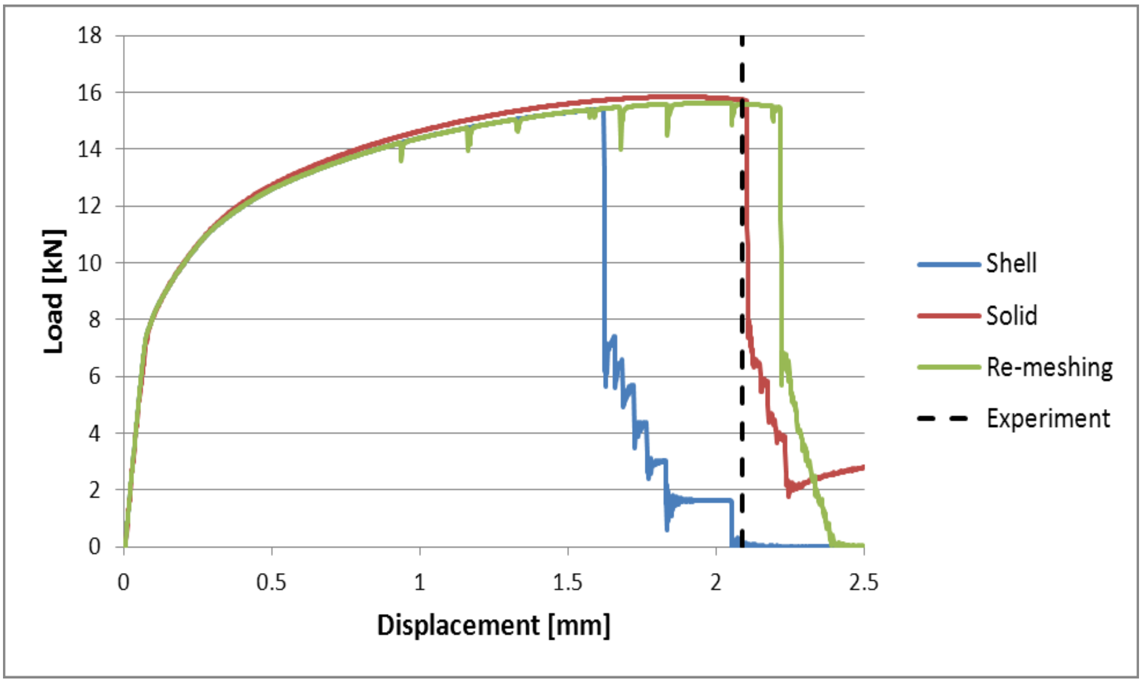

Figure 5-21: Predicted force displacement curve of the central hole tensile test with re-meshing. The experimental instant of fracture is depicted by a dashed black line.

section have been replaced by very fine solid elements. The picture is taken after the onset of fracture (crack initiation), and before the complete failure of the specimen: deleted elements (which correspond to a small crack) can be spotted at the center of the specimen, where the plastic strain is the highest.

Load-displacement curves predicted for the three geometries are depicted in Figs. 5-19 to 5-21. Results using shell elements only (case 1) are in blue, solid elements (case 3) in red and results using re-meshing (case 2) are in green. In all simulations, the abrupt drop of force corresponds to the onset of fracture, while small oscillations visible on the results of simulations using re-meshing (green lines in Figs. 5-19 to 5-21) correspond to re-meshing steps as explained in Section 5.4.2. In addition to the predicted load-displacement curves, the experimental instant of fracture is depicted with a black dashed line for the three geometries. For all geometries, the load-displacement curve features a maximum of force before fracture, which corresponds to the onset of through-the-thickness localization of the stress and strain fields within the specimen gage sections.

For the three fracture experiments considered, simulations using fine solid elements (case 3) predict the instant of fracture with a very good accuracy. As already detailed in section 5.4, simulations using shell elements always under-estimate the fracture displacement. In fact in shell simulations failure occurs just after the maximum of force is reached, as those elements cannot capture correctly the post-necking behavior of the sheet material. When using shell-to-solid re-meshing (green curves in Figs. 5-19 to 5-21), fracture occurs later than when only solid elements are used (red curves). The fracture displacement is over-estimated by 4% for the $6.65mm$ notched tensile specimen, by 7% for the $20mm$ notched tensile specimen and by 5% for the specimen with a central hole. Note that with re-meshing, simulations with initially only shell elements are able to predict correctly the applied load after its maximum.

The evolution of equivalent plastic strain, stress triaxiality and damage at the integration point which fails first are depicted in Figs. 5-22 to 5-24, for the $20mm$ notched tensile specimen. Results from the simulation with solid elements only are shown in red while results using re-meshing are in green. Note that two major re-meshing steps occur in that simulation, the first one at a displacement of about $2.1mm$

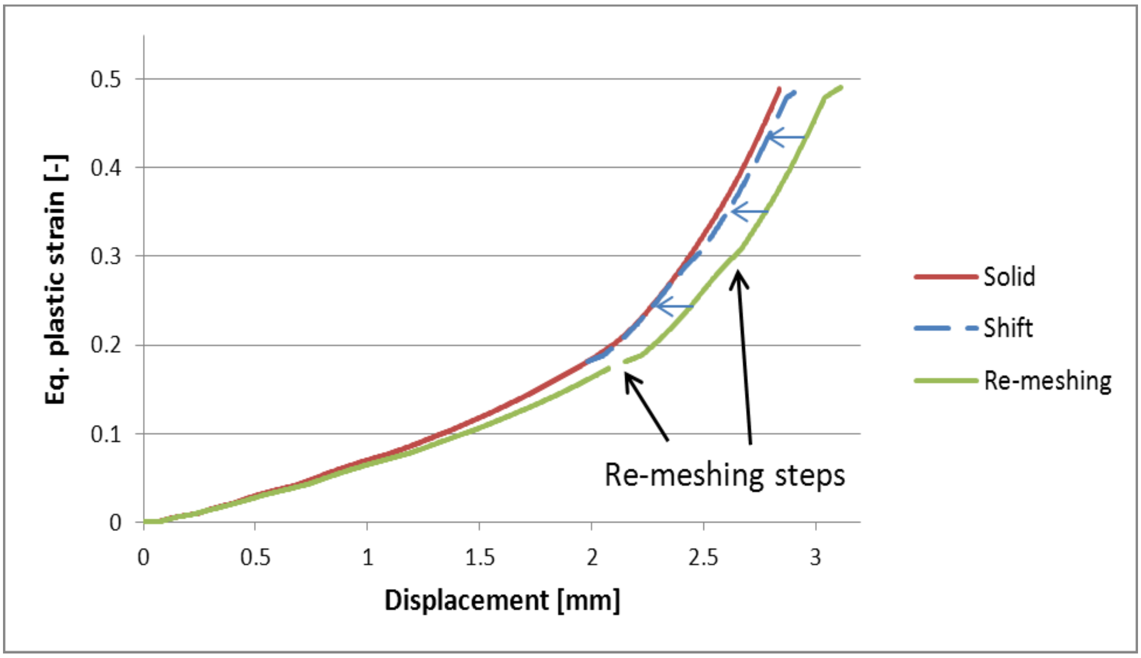

Figure 5-22: Evolution of equivalent plastic strain at the center of the $20mm$ notched tensile specimen, predicted using a solid mesh or re-meshing.

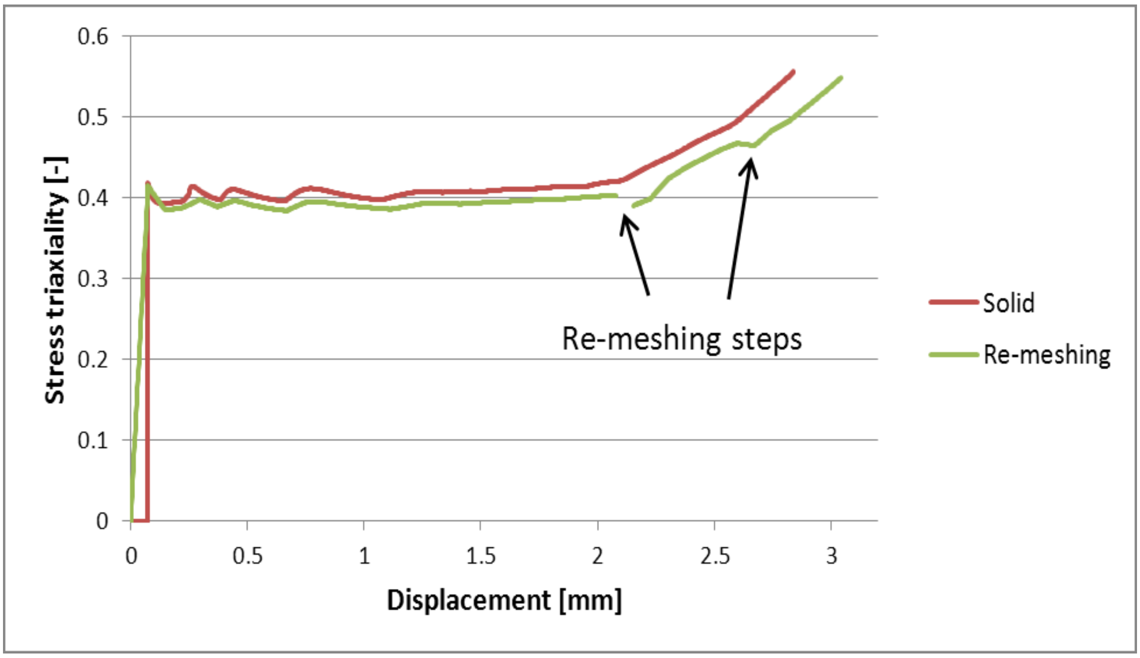

Figure 5-23: Evolution of stress triaxiality at the center of the $20mm$ notched tensile specimen, predicted using a solid mesh or re-meshing.

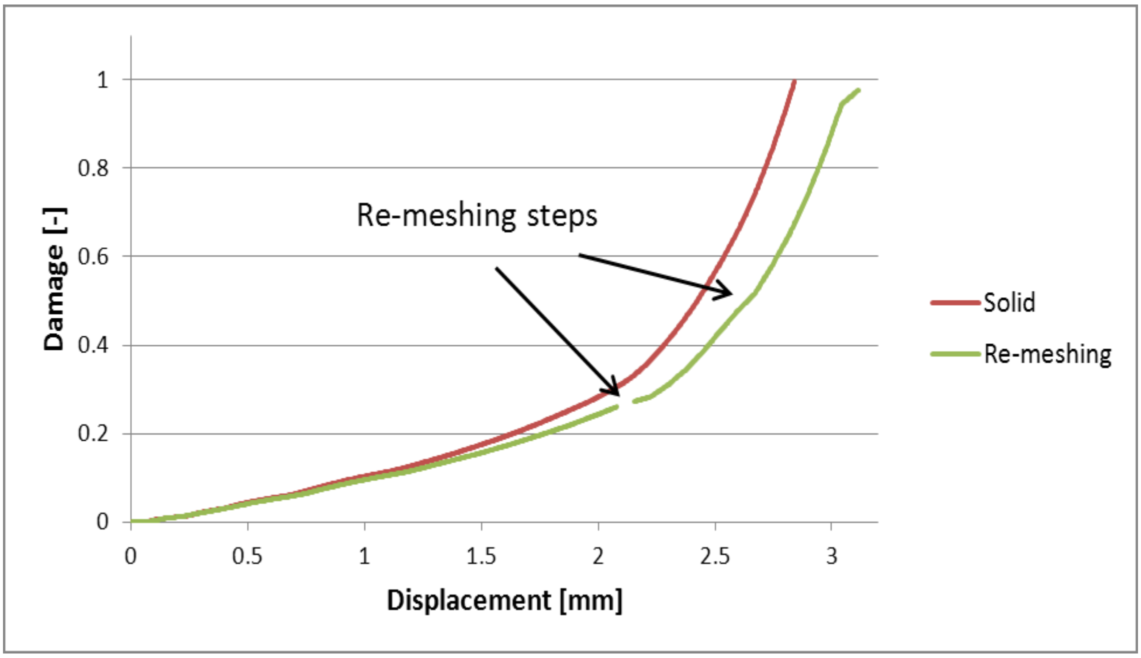

Figure 5-24: Evolution of damage at the center of the $20mm$ notched tensile specimen, predicted using a solid mesh or re-meshing.

where approximately 41,000 solid elements are generated at the center of the gage section, and a second step at a displacement of about $2.6mm$ where 10,000 new solid elements are added to extend the re-meshed area. Before the first re-meshing step, i.e. when only shell elements are present, both the equivalent plastic strain (in Fig. 5-22) and the stress triaxiality (in Fig. 5-23) are underestimated at the center of the gage section compared to results from solid elements (simulation #3, in red). As a result, at the instant of the first re-meshing step, the damage indicator is lower by 15% than in the simulation with only solids. After re-meshing, i.e. when the the center of the specimen gage section is meshed with solid elements, the evolution of equivalent plastic strain is comparable in both simulations: when shifted by the offset due to the inaccuracy of shells, the curve from the re-meshing simulation (in blue in Fig. 5-22) lies almost exactly on top of the curve from the solid simulation (in red in Fig. 5-22). Only a small discrepancy is noticeable at the instant of the second re-meshing step.

The evolution of stress triaxiality (Fig. 5-23) is also slightly underestimated by shell elements before the first re-meshing step. However, unlike for the equivalent plastic strain, differences between the solid simulation and the re-meshing simulation are significant after re-meshing occurred. In particular significant drops of the triaxiality occur at each re-meshing step. Those drops in the stress state correspond to the transient period following the re-meshing step described in Section 5.4.2. In spite of those local drops, it can be noted that the re-meshing simulation is able to capture the increase of triaxialty due to localized necking that occurs before fracture.

Therefore it can be concluded that the over-estimation of the predicted fracture displacement in the simulation with re-meshing is due to under-estimation by shell elements of the plastic strain, stress triaxiality and damage in the early stages of the simulation (before the first re-meshing step) and, to a small extent, to partial unloading that occurs during the subsequent re-meshing steps.

CPU times for the three geometries, using only solid elements and with re-meshing, are summarized in Table 5-4. Note that in all cases, the computation time is reduced by about 75% when re-meshing is used. However it is still much more than when using shell elements only. For all three geometries, the number of generated solid elements is very large compared to the initial number of shells elements. Therefore the computation is controlled by the sub-model containing the generated solids. In case of a simulation of a larger part, where the ratio of generated solids to shell elements would be smaller, it is obvious that the time savings using re-meshing would be greater.

Table 5-4: CPU time (in s) when using re-meshing

Geometry	$6.5mm$ notch	$20mm$ notch	Central hole
Re-meshing	32,300	40,900	52,300
Only solid	126,800	129,800	204,900

5.5 Conclusion

In this chapter, the influence of spacial discretization of Finite Element models on ductile fracture predictions in sheet metals has been investigated. In addition, possible improvements coming from dynamic shell-to-solid re-meshing during the simulations have been assessed.

Based on numerical simulations of a tensile experiment on a flat specimen with circular notches using different element types (both shells and solids) as well as different mesh densities, it has been shown that shells cannot predict the post-necking behavior of sheet materials, regardless of mesh density. As a result spurious localization occurs at the onset of necking, leading to premature failure of the specimen. On the other hand, solids elements are able to predict the through-the-thickness localization that occurs before ductile fracture in AHSS, and thus allow for accurate predictions of the onset of ductile fracture when used in conjunction with suitable fracture initiation models. However very fine meshes (with an element length of about $100\mu m$) are required in order to get converged[8] numerical results: improved accuracy comes at the expense of computational efficiency.

Automatic re-meshing of shell into solid elements is considered to improve the accuracy of simulations with shell elements. The accuracy of the re-meshing technique is evaluated based on numerical simulations of tensile fracture experiments and

[8] In the sense that using a finer mesh would not change the numerical results.

comparison of numerical predictions to experimental results. Concerning the prediction of the onset of ductile fracture, it is shown that simulations with re-meshing are more accurate that those with shell elements only. However, simulations with re-meshing do not match the accuracy of simulations with solid elements only. It is worth mentioning that most of the inaccuracy originates in the first stages of the simulations, before re-meshing when the mesh is composed by shell elements only. In addition, re-meshing permits to predict correctly the post-necking behavior of sheet materials, which cannot be done with shell elements. A correct prediction of local material state of deformation and stress is necessary when trying to predict crack orientation and propagation.